Partially disordered antiferromagnetism and multiferroic behavior in a frustrated Ising system CoCl$_2$-2SC(NH$_2$)$_2$

Eundeok Mun,[1,*] Franziska Weickert,[2] Jaewook Kim,[1,†] Brian L. Scott,[3] Corneliu Florin Miclea,[2,‡] Roman Movshovich,[2] Jason Wilcox,[4] Jamie Manson,[4] and Vivien S. Zapf[1]

[1]*National High Magnetic Field Laboratory, Materials Physics and Applications–Condensed Matter and Magnetic Science, Los Alamos National Laboratory, Los Alamos, New Mexico 87545, USA*
[2]*Materials Physics and Applications–Condensed Matter and Magnetic Science, Los Alamos National Laboratory, Los Alamos, New Mexico 87545, USA*
[3]*Materials Physics and Applications 11, Los Alamos National Laboratory, Los Alamos, New Mexico 87545, USA*
[4]*Department of Chemistry and Biochemistry, Eastern Washington University, Cheney, Washington 99004, USA*
(Received 13 August 2015; revised manuscript received 27 January 2016; published 7 March 2016)

We investigate partially disordered antiferromagnetism in CoCl$_2$-2SC(NH$_2$)$_2$, in which *ab*-plane hexagonal layers are staggered along the *c* axis rather than stacked. A robust 1/3 state forms in applied magnetic fields in which the spins are locked, varying as a function of neither temperature nor field. By contrast, in zero field and applied fields at higher temperatures, partial antiferromagnetic order occurs, in which free spins are available to create a Curie-like magnetic susceptibility. We report measurements of the crystallographic structure and the specific heat, magnetization, and electric polarization down to $T = 50$ mK and up to $\mu_0 H = 60$ T. The Co^{2+} **S** $= 3/2$ spins are Ising-like and form distorted hexagonal layers. The Ising energy scale is well separated from the magnetic exchange, and both energy scales are accessible to the measurements, allowing us to cleanly parametrize them. In transverse fields, a quantum Ising phase transition can be observed at 2 T. Finally, we find that magnetic exchange striction induces changes in the electric polarization up to 3 μC/m^2, and single-ion magnetic anisotropy effects induce a much larger electric polarization change of 300 μC/m^2.

I. INTRODUCTION

The puzzle of frustrated magnetic spins on a triangular lattice has intrigued the scientific community for more than half a century [1]. Classical Ising spins can exist in only two states, and so requiring them to accommodate a threefold lattice with antiferromagnetic interactions is a rich source of interesting magnetic patterns on the micro- and mesoscale. The "up up down" or "up up up" arrangements of Ising spins in a triangle provide the smallest magnetic unit cells. Achieving continuously varying magnetization in the classical Ising scenario requires an infinite series of larger magnetic unit cells, one for each value of the magnetization [2]. One solution to the frustration problem is to avoid static order altogether and form a spin liquid state [3–5]. Another is to form ordering patterns on longer length scales via long-wavelength modulations or phase segregation [6–13]. Finally, partial disorder, where some spins are locked into order and others are free to exhibit Curie behavior, is seen in several triangular-lattice antiferromagnets. Mekata [14] first described the partially disordered antiferromagnet (PDA) on stacked antiferromagnetic triangular lattices. In the PDA state, the chains of ferromagnetically coupled spins form a magnetic state such that two chains are antialigned and one is disordered and free to flip with a low-energy barrier. In the predicted phase

diagram, the PDA state evolves into an "up up down" state with one-third of the saturation magnetization as a function of temperature or magnetic field. Several stacked triangular lattice antiferromagnets show evidence of PDA states and some indication of 1/3 plateaus including members of the ABX_3 and $A_3BB'O_6$ families, among others ($A =$ Ca,Sr; $B =$ Co, Mn,Ni,Ho; $B' =$ Co,Mn,Cr,Rh,Pt,...) [9,10,13–23].

Here we present the compound CoCl$_2$-2SC(NH$_2$)$_2$. We determine its crystal structure, investigate its thermodynamic properties, and construct the magnetic phase diagram down to 50 mK and up to 60 T. This temperature and field range allows us to investigate the phase diagram up to saturation for magnetic fields perpendicular and parallel to the Ising axis, and to quantify the Ising anisotropy. For perpendicular magnetic fields, a transverse Ising scenario applies, allowing us to observe the field-induced quantum phase transition in a transverse Ising model. The structure of this material contrasts with the classic PDA model in that the hexagonal layers in the *ab* plane are staggered, not stacked along the *c* axis. Each spin in a given plane lies at the center of a triangle of spins in the next plane. The lattice is distorted from a perfect triangular lattice, with one bond in each triangle being longer than the other two.

In addition to the magnetic properties, we also investigate multiferroic behavior in this material. The coupling between magnetic and electric long-range order is known as the magnetoelectric multiferroic effect, in which the magnetic order is modified by an electric field and/or the ferroelectricity is modified by a magnetic field [24,25]. Most research to date in multiferroics has focused on transition-metal oxides. Coordination compounds are an alternate route to creating magnetoelectric multiferroic behavior [26–29] with soft and sometimes designable lattice structures. Crystallized organic

---

*Present address: Simon Frazer University, Burnaby, British Columbia, Canada V5A 1S6.

†Present address: Rutgers Center for Emergent Materials, Piscataway, NJ 08854, USA.

‡Present address: National Institute of Materials Physics, 077125 Bucharest-Magurele, Romania.

molecules of thiourea, $SC(NH_2)_2$ [30], and croconic acid, $H_2C_5O_5$ [31], are examples of organic ferroelectrics. The coordination compound $NiCl_2$-$4SC(NH_2)_2$ (DTN) [28] is an example of a thiourea-containing compound in which the polar crystal structure is subject to magnetostriction by magnetically ordered spins, creating magnetoelectric coupling. In the compound studied here, $CoCl_2$-$2SC(NH_2)_2$, two thiourea molecules and two Cl atoms form a tetragonal arrangement around each Co ion. We will show that magnetostrictive distortions due to either exchange interactions or single-ion anisotropy can modify the bulk electric polarization.

II. EXPERIMENT

Single crystals of $CoCl_2$-$2SC(NH_2)_2$ were grown in an ethanol solution with additional isopropanol. Initially, $CoCl_2$ and $SC(NH_2)_2$ were dissolved in warm ethanol in separate glass beakers. After mixing the solutions, additional isopropanol was added. After slow evaporation of the solvent for two weeks, dark blue crystals were obtained. Well-crystallized rod-shaped crystals were obtained with the rod axis oriented along the crystallographic c axis.

X-ray diffraction data were collected in the MPA-11 group at LANL on a Bruker D8 diffractometer, with an APEX II charge-coupled-device (CCD) detector and an American Cryoindustries Cryocool low-temperature device that cooled the sample to 140 K. The instrument was equipped with a graphite monochromatized Mo $K\alpha$ x-ray source ($\lambda = 0.710\,73$ Å) and a 0.5 mm monocapillary. Crystals of $CoCl_2$-$2SC(NH_2)_2$ were mounted in a nylon cryoloop using Paratone-N oil. A hemisphere of data was collected using ω scans, with 10-s frame exposures and 0.5° frame widths. Data collection and initial indexing and cell refinement were handled using APEX II [32] software. Frame integration, including Lorentz-polarization corrections, and final cell parameter calculations were carried out using SAINT+ [33] software. The data were corrected for absorption using redundant reflections and the SADABS [34] program. Decay of reflection intensity was not observed as monitored via analysis of redundant frames. The structure was solved using direct methods and difference Fourier techniques. All hydrogen atoms were assumed to occupy idealized positions relative to the atom that they were attached to. The final refinement included anisotropic temperature factors on all nonhydrogen atoms. Structure solution, refinement, graphics, and the creation of publication materials were performed using SHELXTL [35].

Physical property measurements were performed in the MPA-CMMS group at LANL, which includes the National High Magnetic Field Laboratory Pulsed Field Facility. The temperature and magnetic field dependence of the magnetization, $M(T,H)$, were measured in a quantum design (QD) physical property measurement system (PPMS) with a vibrating sample magnetometer (VSM) option up to $\mu_0 H = 13$ T and down to $T = 2$ K. Below $T = 2$ K, $M(T,H)$ for $\mathbf{H} \parallel \mathbf{c}$ was measured with a capacitive Faraday magnetometer in an Oxford dilution refrigerator in a 12 T superconducting magnet. In addition, $M(H)$ measurements for $\mathbf{H} \parallel \mathbf{c}$ and $\mathbf{H} \perp \mathbf{c}$ were extended up to $\mu_0 H = 60$ T and down to $T = 0.5$ K in resistive pulsed magnets (10 ms rise and 40 ms decay time) driven by a capacitor bank. The pulsed-field magnetization is measured via a compensated induction coil magnetometer [36] with *in situ* sample-in sample-out background subtraction. Samples were immersed in ^{3}He liquid or gas, and their temperature was recorded by a resistive thermometer at zero field just prior to the pulse. The specific heat, $C_p(T)$, of the sample (0.78 mg) was measured by the relaxation technique down to $T = 50$ mK in a QD PPMS with a dilution refrigerator option.

The electric polarization change, $\Delta P(H)$, was measured in pulsed magnetic fields for $\Delta \mathbf{P} \perp \mathbf{c}$ and for both $\mathbf{H} \parallel \mathbf{c}$ and $\mathbf{H} \perp \mathbf{c}$ [27,28]. Platinum contacts were sputtered onto the samples with a cross-sectional area of 1.2×1.25 mm^2 for $\mathbf{H} \perp \mathbf{c}$ and 1.75×2.6 mm^2 for $\mathbf{H} \parallel \mathbf{c}$. The induced magnetoelectric currents (analogous to pyroelectric currents) due to changes in surface charge as P changes with H were recorded with a Stanford Research 570 current to voltage amplifier. Since the magnetoelectric current is proportional to $d\Delta P(t)/dt$, the measured signal is integrated as a function of time to obtain $\Delta P(H)$ with a high sensitivity due to the speed of the pulsed magnetic fields [27,28].

III. RESULTS

A. Crystal structure

The results of single-crystal x-ray scattering and refinement at 140 K are listed in the Supplemental Material [37]. We find the monoclinic structure (Space group $C c$, No. 9, $a = 8.199(1)$ Å, $b = 11.542(2)$ Å, $c = 10.804(2)$ Å, and $\beta = 103.587°$) shown in Fig. 1. The Co ions form a distorted triangular lattice in the ab plane that breaks spatial inversion symmetry and allows for a net electric polarization. The Co ion has C_{2v} point symmetry, and its environment consists of an approximate tetrahedron formed by two Cl atoms and two S atoms, as shown in Fig. 1(b). The bond lengths involving the Co atoms are Co-Cl$_2$ = 2.264(7) Å, Co-Cl$_1$ = 2.284(1) Å, Co-S$_2$ = 2.309(9) Å, and Co-S$_1$ = 2.324(0) Å, and the angles around the Co atoms are Cl$_2$-Co-Cl$_1$ = 107.88(4)° and S$_2$-Co-S$_1$ = 96.85(4)°. The Co-Co distances within the distorted hexagonal ab plane are 7.214(1) Å along two legs of the triangle and 8.199(1) Å along the third, and the angles within a triangle are 55.37(1)°, 55.37(1)°, and 69.26(2)°.
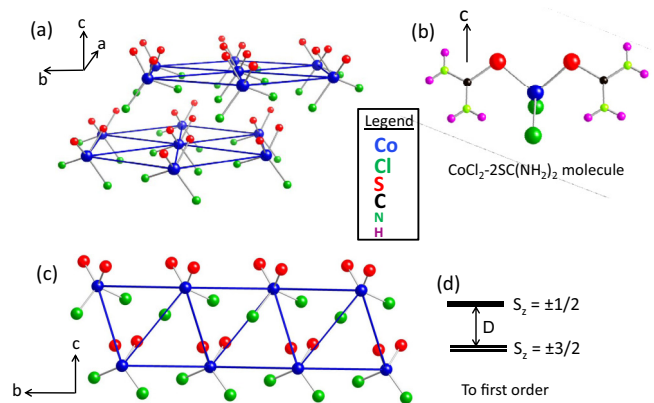

FIG. 1. Crystal structure of $CoCl_2$-$2SC(NH_2)_2$ showing (a) stacking of hexagonal planes (with N and H omitted for clarity), (b) one $CoCl_2$-$2SC(NH_2)_2$ molecule, (c) an a-axis view of the structure (with N and H omitted), and (d) a first-order approximation of the spin level diagram of the Co^{2+} **S** = 3/2 spin levels.
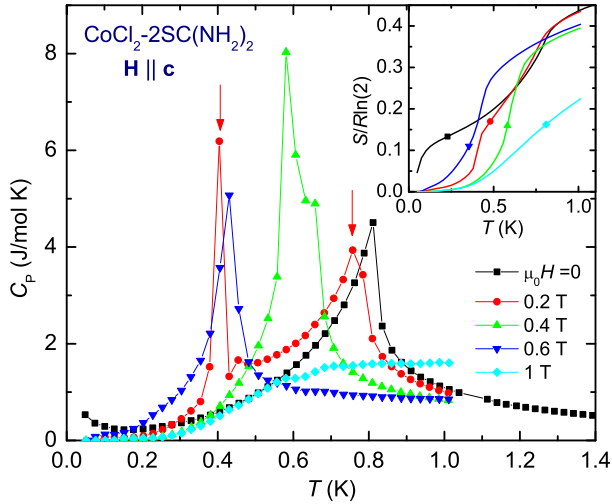
FIG. 2. Specific heat C_p data of CoCl$_2$-2SC(NH$_2$)$_2$, taken at various magnetic fields applied along **H** ∥ **c**. Vertical arrows indicate two phase-transition temperatures for $\mu_0 H = 0.2$ T. The inset shows the calculated total entropy, $S(T)$, in units of $R\ln(2)$ by integrating C/T vs T at various magnetic fields.

FIG. 3. Left axis: C_p/T vs T for $0.05 < T < 4$ K; right axis: $S(T)$ divided by $R\ln(2)$.

B. Specific heat

The specific heat, $C_p(T,H)$, is presented in Fig. 2. At $\mu_0 H = 0$, $C(T)$ exhibits a λ-shaped anomaly at $T_N = 0.82$ K indicating a phase transition. The anomaly centered at 0.82 K shifts to lower T in applied H along the c axis and vanishes by 1 T. For $\mu_0 H = 0.2$ and 0.4 T a second anomaly is also observed, as indicated by arrows in Fig. 2. The entropy change occurring in the phase transitions was estimated by integrating C_p/T as a function of T starting from 50 mK. The entropy change ΔS above 50 mK at several magnetic fields is plotted in the inset of Fig. 2. At these temperatures, the lattice contribution is negligible and the total entropy change is dominated by the magnetic contribution. At $\mu_0 H = 0$, the entropy removed by the long-range ordering is 2.1 J/mol K, which is equivalent to 40% of $R\ln(2)$. We note, however, that there is a small upturn in $C(T)$ as $T \to 0$ for $\mu_0 H = 0$. To investigate this further, in Fig. 3 we plot C/T versus T at $\mu_0 H = 0$ on the left axis and the entropy S on the right axis. The upturn in C and C/T at low T may indicate a divergence of the heat capacity or a second phase transition below $T = 50$ mK. We can rule out a nuclear Schottky anomaly as the origin of this upturn since it vanishes in applied magnetic fields. If indeed the small upturn becomes a tall peak or divergence below 50 mK, it could account for the missing entropy. To achieve $R\ln(2)$ by T_N, the heat capacity below 50 mK would need to reach, e.g., 1.2 J/mol K by 10 mK, and C/T would need to reach 120 J/mol K^2 by 10 mK, which is ten times its value at 50 mK. This scenario cannot be entirely excluded, even though it would require a rather large upturn. In applied magnetic fields, all signs of the upturn in heat capacity at low T vanish, and an entropy of only 35–40% $R\ln(2)$ is recovered by T_N. We can conclude that the observed magnetic ordering is a partial ordering, but an additional transition to full ordering may occur below 50 mK for $H = 0$.
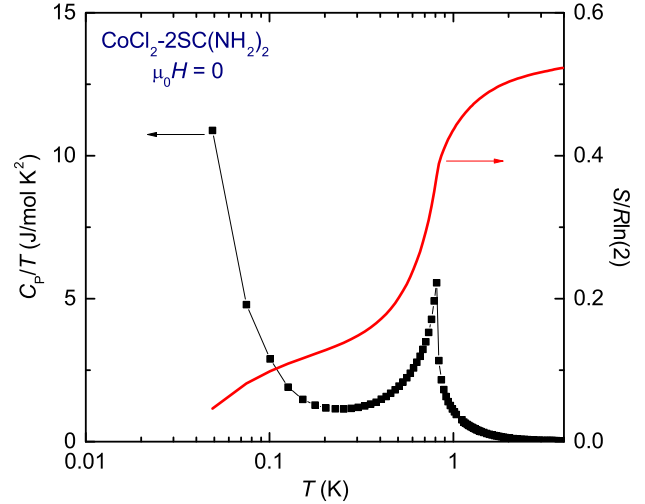
C. Magnetization versus magnetic field

Figure 4(a) shows the magnetization $M(H)$ up to $\mu_0 H = 60$ T in pulsed fields measured for **H** ∥ **c** and **H** ⊥ **c**, calibrated to data taken in a superconducting magnet. The data are reversible between up and down sweeps of the magnetic field, indicating no measurable heating or cooling effects during the magnetic-field pulse. The saturation magnetization by 60 T is 3.5 μ_B/f.u. for **H** ∥ **c** and 2.8 μ_B/f.u. for **H** ⊥ **c**, which is close to the expected value for $S = 3/2$ with minimal orbital contribution. The magnetic field needed to reach saturation is highly anisotropic, being approximately 0.6 T for **H** ∥ **c** and ~40 T for **H** ⊥ **c**.

Given an $S = 3/2$ ion with a Kramer's doublet ground state, there are two possible options for the ground state, regardless of the crystal electric-field environment: an $|S^z = \pm 1/2\rangle$ doublet ground state with an $|S^z = \pm 3/2\rangle$ doublet excited state, or an $|S^z = \pm 3/2\rangle$ doublet ground state with an $|S^z = \pm 1/2\rangle$ doublet excited state. Spin-orbit interactions can also mix the different S^z states, but this can be treated as a higher-order correction for a 3d ion such as Co. In our system, the high-field magnetization data are consistent only with the $|S^z = \pm 3/2\rangle$ ground-state scenario. Thus for the hard axis **H** ⊥ **c**, saturating the magnetization requires ≈40 T to overcome the anisotropy energy and rotate the spins to the hard axis, while for the easy axis **H** ∥ **c** the magnetization saturates by only 0.6 T once the antiferromagnetic order is destroyed. On the other hand, the $|S^z = \pm 1/2\rangle$ ground-state scenario can be ruled out because it would produce saturation fields that are more isotropic. It cannot account for our observed factor of 60 difference between the saturation fields for **H** ∥ **c** and **H** ⊥ **c**. The largest energy scale in our system is the Ising anisotropy energy, and in the $|S^z = \pm 1/2\rangle$ ground-state scenario this energy splitting needs to be overcome via the Zeeman effect in order to reach the $|S_z = 3/2\rangle$ for **H** ∥ **c**, but also in order to reach the $|S_x = 3/2\rangle$ state for **H** ⊥ **c**. ($|S_x = 3/2\rangle$ contains a component of $|S_z = 3/2\rangle$.) Therefore, we conclude that the Co^{2+} $S = 3/2$ ions have an $|S^z = \pm 3/2\rangle$ ground state with strong Ising anisotropy and the easy axis along c. The
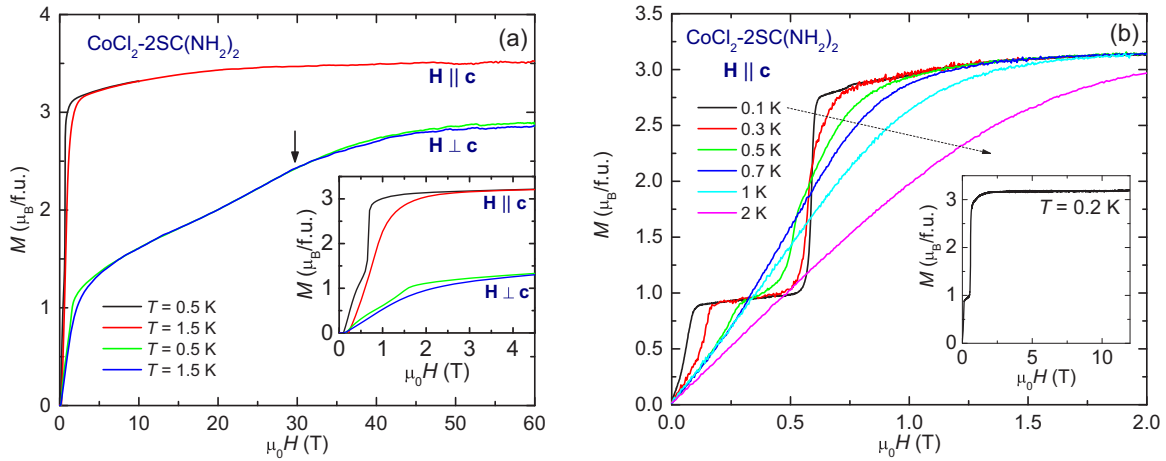
FIG. 4. (a) High-field $M(H)$ for $\mathbf{H} \parallel \mathbf{c}$ and $\mathbf{H} \perp \mathbf{c}$ at $T = 0.5$ and 1.5 K, taken in pulsed magnetic fields up to 60 T. The vertical arrow near $H = 30$ T indicates a slope change in $dM(H)/dH$. The inset shows an expanded scale at low fields. (b) Magnetization isotherms, $M(H)$, of CoCl$_2$-2SC(NH$_2$)$_2$ for $\mathbf{H} \parallel \mathbf{c}$ at selected temperatures. The inset shows $M(H)$ up to 12 T taken at $T = 0.2$ K.

other possibility besides total $\mathbf{S} = 3/2$ is an $\mathbf{S} = 1/2$ total spin with a large g factor due to Van Vleck susceptibility, as can occur in near-octahedral Co^{2+} [38]. However, this scenario is rendered unlikely by the extremely large magnetic anisotropy and the low C_{2v} symmetry of the Co^{2+} environment seen here [39].

Moving on to the low-field behavior of $M(H)$, this is shown in the inset to Fig. 4(a) for pulsed fields for both $\mathbf{H} \parallel$ and $\perp \mathbf{c}$ at $T = 0.5$ and 1.4 K, and also in Fig. 4(b) in a superconducting magnet for $\mathbf{H} \parallel \mathbf{c}$ down to $T = 0.1$ K. The data in the different magnets are consistent with each other. Above $T_N = 0.8$ K in Fig. 4(b), $M(H)$ shows Brillouin-like behavior. Below T_N, $M(H)$ forms a plateau at $1/3 M_{sat}$ for $\mathbf{H} \parallel \mathbf{c}$ and begins to saturate above $\mu_0 H > 0.6$ T with a saturated magnetization of 3.2 μ_B/f.u. The onsets in magnetic field of the 1/3 step and of the saturation correspond to peaks in the heat capacity shown previously.

D. Magnetic susceptibility

The inverse magnetic susceptibility, $H/M(T)$, is plotted in Fig. 5. A fit by a Curie-Weiss law to the data above $T = 100$ K results in a Curie temperature $\theta_p = 11$ K and an effective moment $\mu_{eff} = 4.4 \mu_B$ for $\mathbf{H} \parallel \mathbf{c}$ and $\theta_p = -15$ K and $\mu_{eff} = 4.1 \mu_B$ for $\mathbf{H} \perp \mathbf{c}$, respectively. The moments are in agreement with the expected Co^{2+} ion value with spin $\mathbf{S} = 3/2$. The large anisotropy in the Curie-Weiss temperature, with a sign change from $\mathbf{H} \parallel \mathbf{c}$ to $\mathbf{H} \perp \mathbf{c}$, indicates that the origin of the Curie-Weiss behavior is primarily the single-ion anisotropy while the exchange interactions play a smaller role [40]. This is consistent with the low values of $T_N = 0.8$ K and $H_c = 0.6$ T relative to θ_p.

The low-temperature $M(T)/H$ curves at selected magnetic fields are plotted in the inset of Fig. 5. The $M(T)/H$ curve at $\mu_0 H = 0.05$ T reveals a kink at $T_N = 0.83$ K, below which $M(T)/H$ diverges with decreasing temperature. As the magnetic field increases, T_N shifts to lower temperatures and vanishes between 0.5 and 0.8 T. A second anomaly in the $M(T)/H$ curves is also seen for $0.1 < \mu_0 H < 0.4$ T (see the representative $\mu_0 H = 0.2$ T curve in Fig. 5). This anomaly

corresponds to the second phase transition previously shown in the heat capacity in Fig. 2, which is the onset of the "1/3" state with 1/3 of the saturation magnetization. Figure 5 shows that inside the 1/3 state, the magnetic susceptibility approaches a constant value as $T \to 0$, rather than diverging as it does at $\mu_0 H = 0$.

E. Electric polarization

The electric polarization change, $\Delta P(H)$, for $\mathbf{P} \perp c$ as a function of magnetic field was measured in pulsed magnetic fields up to 60 T. Consistent with the intrinsically polar crystal structure, no dependence on applied voltage up to 200 V is seen before or during measurements. The measurement of magnetoelectric current for $\mathbf{H} \parallel \mathbf{c}$ and $\mathbf{H} \perp \Delta\mathbf{P}$ was performed

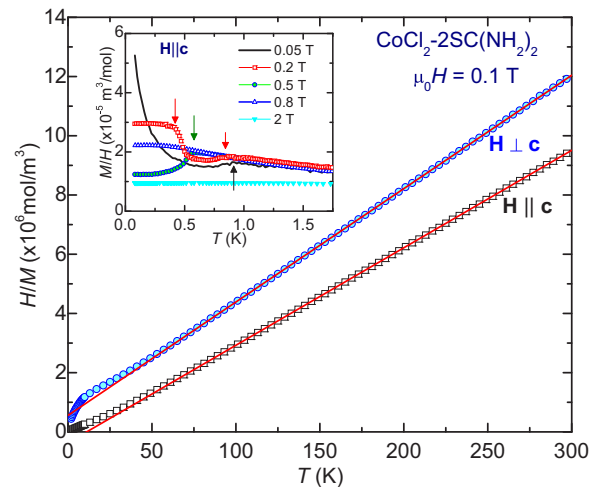FIG. 5. Inverse magnetic susceptibility, $H/M(T)$, of CoCl$_2$-2SC(NH$_2$)$_2$ as a function of temperature for two orientations of the magnetic field: $\mathbf{H} \parallel \mathbf{c}$ and $\mathbf{H} \perp \mathbf{c}$. Solid lines represent a Curie-Weiss fit. The inset shows magnetic susceptibility below $T = 1.75$ K at selected magnetic fields applied along $\mathbf{H} \parallel \mathbf{c}$. Phase-transition temperatures, determined by $d[(M/H)T]/dT$, are indicated by arrows.
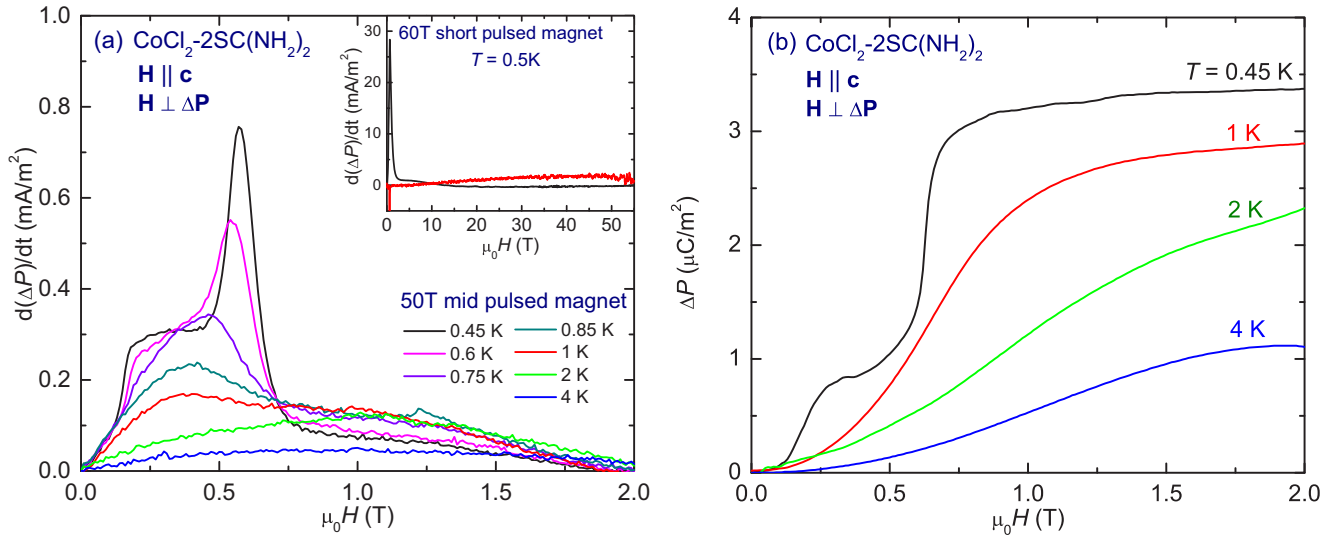
FIG. 6. (a) Electric polarization change with time, $d\Delta P/dt$, plotted as a function of magnetic field $\mu_0 H$ at various temperatures, where $\mathbf{H} \parallel \mathbf{c}$ and $\mathbf{H} \perp \Delta\mathbf{P}$. The inset shows $d\Delta P/dt$ at $T = 0.5$ K up to $\mu_0 H = 60$ T. (b) $\Delta P(H)$ determined by integrating $d\Delta P/dt$ as a function of time.

in a slow capacitor-driven pulsed field magnet (40 ms rising and 250 ms falling time) up to 5 T, and in a faster capacitor-driven pulsed magnet (10 ms rising and 40 ms falling time) up to 60 T. The measured magnetoelectric current, $d(\Delta P)/dt$, induced by the polarization change of the sample and the integrated signal, $\Delta P(H)$, are plotted in Figs. 6(a) and 6(b) for $\mathbf{H} \parallel \mathbf{c}$, and in Figs. 7(a) and 7(b) for $\mathbf{H} \perp \mathbf{c}$, respectively, where $\Delta\mathbf{P} \perp \mathbf{c}$ for both orientations of the magnetic field. The difference in magnitude of the raw $d(\Delta P)/dt$ data between Fig. 6(a) and the inset is due to the different magnetic field sweep rates. This sweep-rate dependence is absent for the integrated $\Delta P(H)$ curves.

$\Delta P(H)$ in Fig. 6 shows features consistent with $M(H)$ for both magnetic-field directions. For $\mathbf{H} \parallel \mathbf{c}$, a 1/3 plateau is

seen in $P(H)$ similar to $M(H)$ at $T = 0.45$ K. For $T > T_N$, $\Delta P(H)$ evolves smoothly and monotonically without any noticeable anomalies, and the magnitude is immediately suppressed above T_N. For $\mathbf{H} \perp \mathbf{c}$, a kink in $d(\Delta P)/dt$ appears at $\mu_0 H = 1.5$ T corresponding to the suppression of long-range order [see the inset to Fig. 7(a)], and a drastic change occurs near $\mu_0 H = 30$ T. The integrated $P(H)$ shows a large peak at 30 T, which is just below the field where the magnetization begins to saturate. The same behavior is seen for both rising and falling field sweeps, except for a small hysteresis at the phase transition near $\mu_0 H = 1.5$ T. The observed amplitude of $\Delta P(H)$ at the phase transition is similar for both $\mathbf{H} \parallel \mathbf{c}$ and $\mathbf{H} \perp \mathbf{c}$, whereas $\Delta P(H)$ around $\mu_0 H = 30$ T along $\mathbf{H} \perp \mathbf{c}$ is $\sim$100 times bigger.
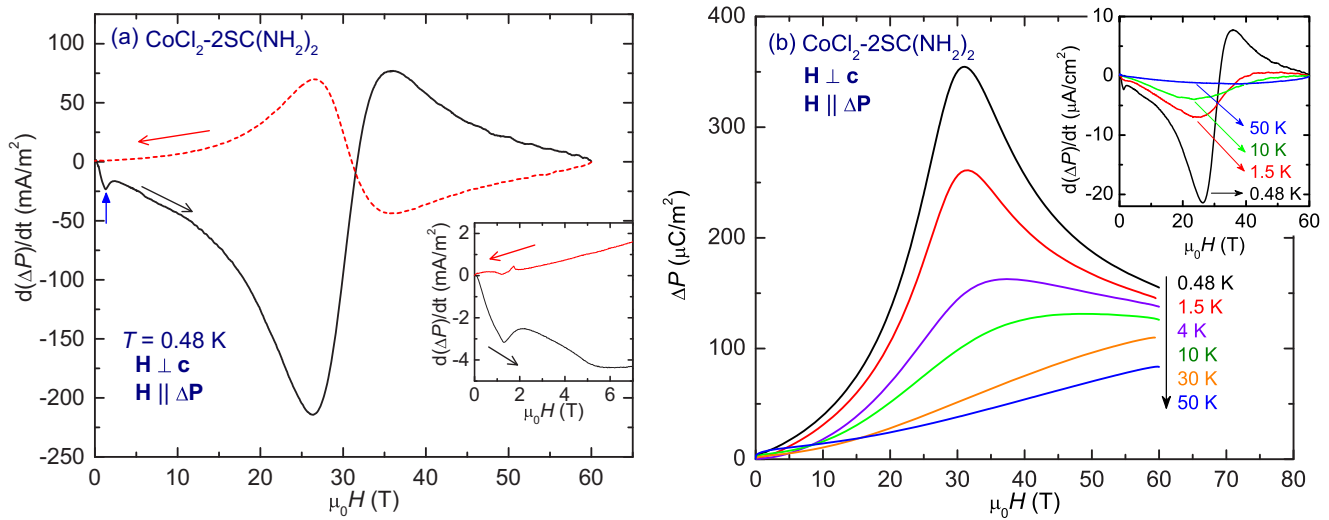

FIG. 7. (a) Electric polarization change, $d\Delta P/dt$ vs magnetic field $\mu_0 H$, at $T = 0.48$ K for $\mathbf{H} \perp \mathbf{c}$. The inset shows an expanded plot up to $\mu_0 H = 10$ T. The vertical arrow indicates a phase-transition field, and horizontal arrows indicate up-sweep and down-sweep. (b) $\Delta P(H)$ determined at various temperatures by integrating $d\Delta P/dt$ as a function of time. The inset shows $d\Delta P/dt$ at selected temperatures.
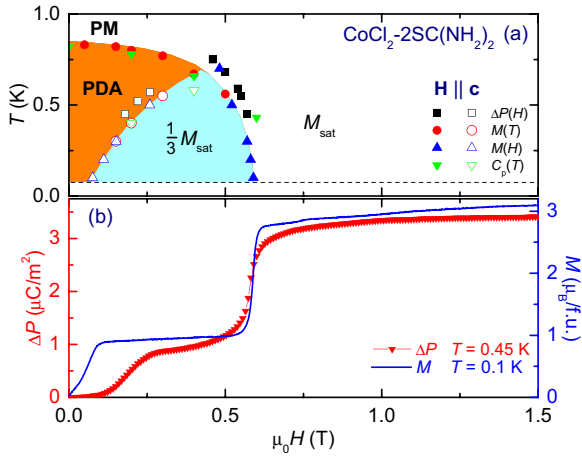
FIG. 8. (a) The H-T phase diagram of $CoCl_2$-$2SC(NH_2)_2$ for **H** ∥ **c**, obtained from magnetization, specific heat, and electric polarization measurements. Phases are indicated as paramagnetic (PM), partially disordered antiferromagnet (PDA), $1/3 M_{sat}$, and M_{sat} for the phase approaching saturation. (b) The electric polarization change $\Delta P(H)$ (left axis) at $T = 0.45$ K, and magnetization $M(H)$ (right axis) at $T = 0.1$ K, which are the respective base temperatures of measurements.

IV. DISCUSSION

The magnetic ordering in $CoCl_2$-$2SC(NH_2)_2$ for **H** ∥ **c** is bounded by $T = 0.83$ K and $\mu_0 H = 0.6$ T. The phase diagram obtained by the present measurements is shown in Fig. 8(a), where the phase boundaries were determined from the peak position in $d\{[M(T)/H]T\}/dT$, $dM(H)/dH$, $d[\Delta P(H)]/dH$, and the peak position of $C_p(T)$. The phase diagram and magnetic behavior are consistent with a PDA model [14]. In the zero-field partially disordered state, the magnetic susceptibility diverges at low temperatures, indicating some free spins that exhibit a Curie behavior. In this phase, only ∼40% of the expected entropy for fully ordering the spins is observed from the specific-heat measurements, indicating partial disorder. A <50 mK transition to full order, only at $H = 0$, cannot be ruled out, and it may be an additional feature of this phase diagram. Upon applying a field, a phase transition to the 1/3 magnetization phase is observed in the heat capacity, magnetization, and electric polarization measurements. In this phase with 1/3 of the saturation magnetization, the Curie-like magnetic susceptibility disappears and the magnetization at low temperatures approaches a constant value—all spins lock into the 1/3 state. The 1/3 magnetization holds over an extended region of the T-H phase diagram with no observable change in magnetization with temperature or field. This behavior is an especially pronounced example of the behavior expected from Ising spins in a PDA model. The magnetic field required to order the disordered spins and induce the 1/3 state extrapolates close to $\mu_0 H = 0$ at $T = 0$, indicating minimal energy barriers for flipping the free spins. Given Ising spins on a lattice with threefold symmetry (approximately satisfied for this compound), an "up up down" configuration within triangles is the most likely ordering. With further increasing field, the spins undergo a second field-induced phase transition out of this locked 1/3 state and then evolve toward saturation at $3 \mu_B$.

An important difference between this material and other PDA materials is a lack of 1D chains in the crystal structure. The classic PDA model [14] is postulated for strongly correlated ferromagnetic chains of spins that are weakly coordinated in a triangular motif in the perpendicular direction. In $CoCl_2$-$2SC(NH_2)_2$, the crystal structure does not evidence such chains—the hexagonal layers are staggered, not stacked. A spin in one plane is bonded to three spins in the next plane, forming a tetrahedron. Thus it is a geometrically different example of partial antiferromagnetic ordering due to triangular frustration [9,10,13,15–23].

We can quantify the degree of Ising-ness of the Co spins from the anisotropy between the saturation magnetic field for the easy **c** axis (0.6 T) and the hard axis perpendicular to c (40 T). The scenario consistent with the data is for the Co^{2+} **S** = 3/2 spins to be split into an $|S^z = \pm 3/2\rangle$ Kramer's protected ground state, with an excited $|S^z = \pm 1/2\rangle$ state separated by an energy gap D [Fig. 1(d)]. For **H** ∥ **c**, saturation is reached for low fields (as soon as the effects of magnetic exchange interactions J are overcome by 0.6 T), while saturating the magnetization for **H** ⊥ **c** requires mixing components of $|S_z = \pm 3/2\rangle$ and $|S_z = \pm 1/2\rangle$ to achieve the $|S_x = 3/2\rangle$ state. Thus the gap D must be closed to reach **H** ⊥ **c** saturation near 40 T, and so we estimate $D \sim 60$ K along the c axis, assuming $g = 2$ and **S** = 3/2.

Our conclusions can be summarized by a Hamiltonian of the form $H = \sum_{r,v} J_v \mathbf{S_r} \cdot \mathbf{S_{r+e_v}} + \sum_r [D(S_r^z)^2 - g \mu_B \mathbf{S_r^z} \cdot \mathbf{H}]$, where J_v are the magnetic exchange constants, D is the single-ion anisotropy due to a uniaxial crystal electric field along the c axis, and $\mathbf{e}_v = (a\hat{x}, b\hat{y}, x\hat{z})$ are the relative vectors between nearest-neighbor Co ions connected by magnetic exchange interactions.

A comparison of the saturation fields of 0.6 T along the easy axis (needed to overcome antiferromagnetic exchange interactions) and 40 T along the hard axis (needed to overcome single-ion anisotropy) indicates that this material is in the limit of large D/J with an Ising energy scale approximately 10 times larger than the magnetic exchange. A consequence of the large D/J limit is that the Curie-Weiss behavior of the magnetic susceptibility is dominated by single-ion anisotropy and not by magnetic exchange [40]. Consistent with this, the Curie-Weiss temperature changes sign when the magnetic field is rotated from the easy to the hard axis (-15 K versus $+11$ K).

For the magnetic field **H** ⊥ **c**, a transverse Ising scenario applies. The magnetization shows three different slopes, between $0 \leqslant \mu_0 H \leqslant 2$ T, $2 \leqslant \mu_0 H \leqslant 40$ T, and $40 \leqslant \mu_0 H \leqslant 60$ T. For lower fields, we can expect the magnetization to be influenced by spin-flip excitations (superposition states of $|S^z = 3/2\rangle$ and $|S^z = -3/2\rangle$). A phase transition near 2 T at 0.5 K in $M(H)$ is observed in Fig. 4, which would be a field-induced quantum phase transition of the transverse Ising model [41–43]. Further investigation of transverse Ising behavior in this system is a future project requiring a detailed understanding of the exchange couplings. The final saturation near 60 T is given by the energy scale needed to overcome D, the gap between the ground state $|S^z = \pm 3/2\rangle$ and the excited $|S^z = \pm 1/2\rangle$ states.

Coupling between magnetism and electric polarization is shown in Fig. 8(b). $CoCl_2$-$2SC(NH_2)_2$ has an intrinsically polar crystal structure that allows for a net electric polarization

starting at high temperatures (confirmed at 140 K). Any magnetostriction-induced changes in the lattice parameters can therefore modify the electric polarization, regardless of the symmetry of the magnetic order. In general, the quantities D and J depend on the arrangement of atoms within the crystal structure. Thus, the system will modify these through magnetostriction to minimize the combination of magnetic and crystalline energy. In the data, we observe that in the region of magnetic ordering, $\Delta P(H)$ exhibits similar magnetic field evolution to that of the magnetization, including a 1/3 plateau and paramagnetic behavior just above T_N. The magnitude of ΔP is 3 μC/m^2 for $\mathbf{H} \parallel \mathbf{c}$ due to magnetic exchange striction. Much larger values of $\Delta P(H)$ are seen for $\mathbf{H} \perp c$ at higher magnetic fields up to 60 T. We can attribute these to magnetostriction driven by the single-ion D term in the Hamiltonian. The value of $\Delta P(H)$ is 300 μC/m^2, which is within a factor of 10 of the largest magnetic field-induced electric polarization changes observed in multiferroic materials [44,45]. The thiourea-containing compound NiCl$_2$-4SC(NH$_2$)$_2$ also shows magnetoelectric coupling due to both D and J terms, albeit with a smaller magnitude. A detailed experimental and theoretical analysis of these effects is presented in Ref. [28].

V. SUMMARY

Single crystals of a new coordination compound CoCl$_2$-2SC(NH$_2$)$_2$ have been synthesized. The compound has a distorted hexagonal structure and shows magnetic ordering consistent with a partially disordered antiferromagnetic state at $\mu_0 H = 0$, where two spins order and one remains disordered in a triangular motif. In applied magnetic fields, a locked 1/3 state occurs, where the magnetization remains constant at 1/3 of the saturation magnetization over a remarkably broad region in temperature and magnetic fields. The geometry of this compound differs from that of usual partially disordered antiferromagnets since it shows staggered hexagonal planes, rather than the usual c-axis spin chains in a triangular configuration. The Co^{2+} $\mathbf{S} = 3/2$ spins form a doublet ground state with $|S^z = \pm 3/2\rangle$ and an easy-axis anisotropy axis along the crystallographic c axis. The well-separated energy scales for magnetic ordering and anisotropy make this a clean Ising system. In addition, this material shows an electric polarization that is strongly coupled to magnetization with a magnetic field-induced polarization change up to 300 μC/m^2. The largest electric polarization changes in this material are produced by the single-ion anisotropy effect creating magnetically driven distortions of the Co environment.

[1] G. H. Wannier, Phys. Rev. **79**, 357 (1950).

[2] K. Nakanishi, J. Phys. Soc. Jpn. **52**, 2449 (1983).

[3] L. Balents, Nature (London) **464**, 199 (2010).

[4] S. Nakatsuji, Y. Nambu, H. Tonomura, O. Sakai, S. Jonas, C. Broholm, H. Tsunetsugu, Y. Qiu, and Y. Maeno, Science **309**, 1697 (2005).

[5] P. W. Anderson, Mater. Res. Bull. **8**, 153 (1973).

[6] P. Bak, Rep. Prog. Phys. **45**, 587 (1982).

[7] W. Selke, Phys. Rep. **170**, 213 (1988).

[8] S. Kobayashi, S. Mitsuda, M. Ishikawa, K. Miyatani, and K. Kohn, Phys. Rev. B **60**, 3331 (1999).

[9] S. Agrestini, L. C. Chapon, A. Daoud-Aladine, J. Schefer, A. Gukasov, C. Mazzoli, M. R. Lees, and O. A. Petrenko, Phys. Rev. Lett. **101**, 097207 (2008).

[10] S. Agrestini, C. Mazzoli, A. Bombardi, and M. R. Lees, Phys. Rev. B **77**, 140403 (2008).

[11] S. A. J. Kimber, H. Mutka, T. Chatterji, T. Hofmann, P. F. Henry, H. N. Bordallo, D. N. Argyriou, and J. P. Attfield, Phys. Rev. B **84**, 104425 (2011).

[12] K. Prsa, M. Laver, M. Mansson, S. Guerrero, P. M. Derlet, I. Zivkovic, H. T. Yi, L. Porcar, O. Zaharko, S. Balog, J. L. Gavilano, J. Kohlbrecher, B. Roessli, C. Niedermayer, J. Sugiyama, C. Garcia, H. M. Ronnow, C. Mudry, M. Kenzelmann, S. W. Cheong, and J. Mesot, arXiv:1404.7398.

[13] C. L. Fleck, M. R. Lees, S. Agrestini, G. J. McIntyre, and O. A. Petrenko, Europhys. Lett. **90**, 67006 (2010).

[14] M. Mekata, J. Phys. Soc. Jpn. **42**, 76 (1977).

[15] H. Hori, H. Mikami, M. Date, and K. Amaya, Physica B **165–166**, 237 (1990).

[16] V. Hardy, M. R. Lees, O. A. Petrenko, D. M. Paul, D. Flahaut, S. Hébert, and A. Maignan, Phys. Rev. B **70**, 064424 (2004).

[17] S. Niitaka, K. Yoshimura, K. Kosuge, M. Nishi, and K. Kakurai, Phys. Rev. Lett. **87**, 177202 (2001).

[18] S. Niitaka, H. Kageyama, K. Yoshimura, K. Kosuge, S. Kawano, N. Aso, A. Mitsuda, H. Mitamura, and T. Goto, J. Phys. Soc. Jpn. **70**, 1222 (2001).

[19] N. Mohapatra, K. K. Iyer, S. Rayaprol, and E. V. Sampathkumaran, Phys. Rev. B **75**, 214422 (2007).

[20] V. Hardy, C. Martin, G. Martinet, and G. André, Phys. Rev. B **74**, 064413 (2006).

[21] Y. Nishiwaki, M. Tokounaga, N. Todoroki, and T. Kato, J. Phys. Soc. Jpn. **82**, 104717 (2013).

[22] E. Lefrancois, L. C. Chapon, V. Simonet, P. Lejay, D. Khalyavin, S. Rayaprol, E. V. Sampathkumaran, R. Ballou, and D. T. Adroja, Phys. Rev. B **90**, 014408 (2014).

[23] S. F. Jin, Q. Huang, Z. P. Lin, Z. L. Li, X. Z. Wu, T. P. Ying, G. Wang, and X. L. Chen, Phys. Rev. B **91**, 094420 (2015).

[24] J. F. Scott, Rep. Prog. Phys. **42**, 1055 (1979).

[25] M. Fiebig, J. Phys. D **38**, R123 (2005).

[26] P. Jain, V. Ramachandran, R. J. Clark, H. D. Zhou, B. H. Toby, N. S. Dalal, H. W. Kroto, and A. K. Cheetham, J. Am. Chem. Soc. **131**, 13625 (2009).

[27] V. S. Zapf, M. Kenzelmann, F. Wolff-Fabris, F. Balakirev, and Y. Chen, Phys. Rev. B **82**, 060402 (2010).

[28] V. S. Zapf, P. Sengupta, C. D. Batista, F. Nasreen, F. Wolff-Fabris, and A. Paduan-Filho, Phys. Rev. B **83**, 140405 (2011).

[29] Y. Tian, A. Stroppa, Y. Chai, L. Yan, S. Wang, P. Barone, S. Picozzi, and Y. Sun, Sci. Rep. **4**, 6062 (2014).

[30] G. J. Goldsmith and J. G. White, J. Chem. Phys. **31**, 1175 (1959).

[31] S. Horiuchi, Y. Tokunaga, G. Giovannetti, S. Picozzi, H. Itoh, R. Shimano, R. Kumai, and Y. Tokura, Nature (London) **463**, 789 (2010).

[32] APEX II 1.08, 2004, Bruker AXS, Inc., Madison, WI 53719.

[33] SAINT+ 7.06, 2003, Bruker AXS, Inc., Madison, WI 53719.

[34] SADABS 2.05, 2002, George Sheldrick, University of Gottingen, Germany.

[35] SHELXTL 5.10, 1997, Bruker AXS, Inc., Madison, WI 53719.

[36] J. A. Detwiler, G. M. Schmiedeshoff, N. Harrison, A. H. Lacerda, J. C. Cooley, and J. L. Smith, Phys. Rev. B **61**, 402 (2000).

[37] See Supplemental Material at http://link.aps.org/supplemental/10.1103/PhysRevB.93.104407 for a cif file with the results of structure refinement, as well as the magnetic field versus time profiles and sweep rates of the pulsed magnets used in this study.

[38] S. Kimura, H. Yashiro, K. Okunishi, M. Hagiwara, Z. He, K. Kindo, T. Taniyama, and M. Itoh, Phys. Rev. Lett. **99**, 087602 (2007).

[39] M. Idesicova, L. Dlhan, J. Moncol, J. Titis, and R. Boca, Polyhedron **36**, 79 (2012).

[40] W. Fernengel and H. Kronmuller, J. Magn. Magn. Mater. **13**, 211 (1979).

[41] M. Ronnow, R. Parthasarathy, J. Jensen, G. Aeppli, T. F. Rosenbaum, and D. F. McMorrow, Science **308**, 389 (2005).

[42] R. Coldea, D. A. Tennant, E. M. Wheeler, E. Wawrzynska, D. Prabhakaran, M. Telling, K. Habicht, P. Smeibidl, and K. Kiefer, Science **327**, 177 (2010).

[43] A. Dutta, U. Divakaran, D. Sen, B. K. Chakrabarti, T. F. Rosenbaum, and G. Aeppli, arXiv:1012.0653.

[44] J. W. Kim, S. Artyukhin, E. D. Mun, M. Jaime, N. Harrison, A. Hansen, J. J. Yang, Y. S. Oh, D. Vanderbilt, V. S. Zapf, and S.-W. Cheong, Phys. Rev. Lett. **115**, 137201 (2015).

[45] R. D. Johnson, L. C. Chapon, D. D. Khalyavin, P. Manuel, P. G. Radaelli, and C. Martin, Phys. Rev. Lett. **108**, 067201 (2012).